Construction and Building Materials 400 (2023) 132547

Contents lists available at ScienceDirect

Construction and Building Materials

journal homepage: www.elsevier.com/locate/conbuildmat

The influence of density on the fracture energy of AAC: From experimental investigation to the calibration of a cohesive law

E. Michelini [a,*], D. Ferretti [a], M. Pizzati [b]

[a] Department of Engineering and Architecture, University of Parma, P.co Area delle Scienze 181/A, 43124 Parma, Italy
[b] Department of Chemistry, Life Sciences and Environmental Sustainability, University of Parma, P.co Area delle Scienze 157/A, 43124 Parma, Italy

ARTICLE INFO

Keywords:
Autoclaved aerated concrete
Experimental tests
Fracture energy
Cohesive law
Fictitious crack model
Neural networks
Density
Porosity

ABSTRACT

The paper investigates cracking development in Autoclaved Aerated Concrete (AAC) elements, and clarifies the effect of density and porosity on material mechanical properties. To this purpose, 4 material densities are analyzed, ranging from 300 kg/m^3 to 580 kg/m^3, corresponding to a compressive strength interval approximately ranging from 1.90 MPa to 5.50 MPa. Fracture mechanics of AAC is analyzed by carrying out three-point bending tests on notched beams, similar to those commonly used for normal concrete elements. In these tests, the onset and development of crack pattern is studied by means of Digital Image Correlation technique. An almost linear dependence of fracture energy from density (and consequently from strength) is derived based on test results. Experimental results are used to calibrate a bi-linear cohesive law, whose parameters vary with material density, so allowing to differentiate fracture properties for structural (high density) and non-structural (low density) AAC elements in finite element analyses. The cohesive law parameters are calibrated by exploiting a neural network algorithm and interfacing MatLab with ABAQUS Finite Element package. The curves obtained for the 4 investigated densities, normalized with respect to material tensile strength, are almost superimposed on each other as if the stresses were scaled with porosity. The displacements corresponding to the knee of the curve are nearly coincident, independently from material density. The good agreement between experimental and numerical results proves the reliability of the proposed approach.

1. Introduction

Autoclaved Aerated Concrete (AAC) is a porous lightweight material that offers interesting heat insulation properties combined with good mechanical performances [1–5]. This combination of thermal and structural efficiency makes AAC an attractive choice for the building industry, also by virtue of the growing interest shown by public opinion with regard to the problem of global warming and the need to cut carbon dioxide emissions [6]. The use of AAC for the realization of load-bearing walls and/or for infills in framed structures reduces indeed the need for additional insulation products, with consequent advantages in terms of stability, construction costs and environmental impact [7–9]. Moreover, the thermal efficiency of AAC products sharply reduces the need for space heating and cooling, with a consequent noticeable reduction of energy consumption in residential and industrial buildings [5,10–12].

One of the main drawbacks of AAC is its inherent brittleness, which makes it prone to cracking under both static and dynamic loads [13–15]. As for ordinary concrete, fracture toughness of AAC can be improved through the addition of fibers; however, their application is still limited due to the following twofold reasons: 1) only some types of fibers are suitable for the production process of AAC; 2) fiber addition often causes an undesirable reduction of thermal insulation performances [14,16,17]. As a consequence, the knowledge of fracture mechanics parameters becomes relevant to quantify material brittleness for improving its properties, as well as to perform reliable numerical simulations of damage evolution in plain AAC elements and structures [18]. For quasi-brittle materials like concrete and AAC, it is generally recognized the validity of the fictitious crack model introduced by Hillerborg and others [19], on the basis of the cohesive crack model firstly proposed by Barenblatt [20] and then improved by Rice [21]. Hillerborg's model assumes that the fracture zone can be treated as a fictitious crack able to transfer stresses to a certain extent, in relation to crack opening (i.e., when crack opening becomes too large, stresses are no longer transmitted). To describe the stress transmission across the fictitious crack, a cohesive law should be therefore introduced, representing the behavior of the material softened by microcracking. The cohesive law is

* Corresponding author.
E-mail address: elena.michelini@unipr.it (E. Michelini).

https://doi.org/10.1016/j.conbuildmat.2023.132547
Received 11 April 2023; Received in revised form 11 July 2023; Accepted 16 July 2023
Available online 28 July 2023
0950-0618/© 2023 The Author(s). Published by Elsevier Ltd. This is an open access article under the CC BY-NC-ND license (http://creativecommons.org/licenses/by-nc-nd/4.0/).

generally provided in the form of a stress vs. crack opening displacement relation, and its definition requires the knowledge of some main material properties, like the tensile strength f_t and the fracture energy G_F, which can be intended as the area under the $\sigma - w$ curve. The knowledge of cohesive law parameters is the key to perform reliable Nonlinear Finite Element (FE) simulation on the investigated material.

With respect to other mechanical properties, fracture mechanics parameters of AAC have been so far less investigated in the literature [22–26]. Experimental data on direct tensile strength are usually hardly available due to the difficulties in test execution, which are mainly connected to the possible cracking of the specimen at grips [27]. For this reason, similarly to standard concrete, also for AAC splitting tensile tests or Three-Point Bending (TPB) tests are routinely performed by researchers to provide an estimate of material tensile strength (i.e., among others, [26,28–30]). From these tests, it is also possible to indirectly derive direct tensile strength, by means of ESPI technique and inverse Finite Element (FE) analysis, as discussed in Ferretti et al. [26]. However, it should be observed that the strength of AAC significantly depends on the viscousness, as well as on the shape and size of the samples, as discussed in [31]. As regards fracture energy, RILEM recommendation AAC 13.1 [32] suggests the execution of wedge-splitting tests, which consist in pressing two wedges symmetrically in order to split the specimen into two halves. However, the test setup discussed in [32] has some drawbacks and for this reason some alternatives can be found in the literature [25]. One of the main modifications to the test setup consists in placing the specimen over two symmetric line supports, instead of only one-line support in the center, so to avoid a multiaxial stress distribution at the end of the crack path, which affects the cohesive law. When performing wedge-splitting tests, the splitting force is first calculated starting from the applied vertical load and the wedge angle, and then the fracture energy G_F is determined as the area under the splitting force − Crack Mouth Opening Displacement (CMOD) curve, divided by the ligament area A_{lig} [25]. Another common experimental procedure to determine fracture energy in cementitious materials is represented by TPB tests on notched beams [33,34], which are easier to be controlled thanks to their simpler setup. Previous studies (e.g. [35]) have proved that, irrespective of the specimen shape, identical G_F values can be obtained from TPB tests and wedge-splitting ones, providing that the ligament length and the cementitious material are the same. For this reason, Three-Point-Bending (TPB) tests on notched specimens under CMOD control have been successfully extended also to AAC specimens, as discussed in [26,30]. In this case, the fracture energy G_F can be determined by calculating either the area under the load - CMOD curve (by introducing a correction factor equal to 0.75, [34]), or the area under the load-midspan deflection curve, if the latter is measured during the test by means of a Linear Variable Displacement Transducer (LVDT) or through non-contact methods, such as the Digital Image Correlation (DIC) technique. In both cases, it is necessary to divide the above-mentioned areas by the ligament area A_{lig}.

So far, the available works in the literature on this topic are quite limited, and, to the Authors' knowledge, published studies on the variation of the cohesive law with material density and compressive strength - which is correlated to the density - are still missing. For this reason, the present paper experimentally investigates the dependency of fracture energy from density and porous structure of AAC, by analyzing four AAC density classes (corresponding to a compressive strength interval approximately ranging from 1.90 MPa to 5.50 MPa), and the obtained results are then elaborated to calibrate cohesive law parameters, so to clarify their possible dependence from material density and strength. This allows to provide reliable data to be used in FE simulations not only for load-bearing masonry (with higher densities), but also for lower density products (such as infills and cladding), through a differentiation of fracture properties for AAC used in structural and non-structural applications. To achieve this goal, TPB tests on both un-notched and notched specimens belonging to 4 different density grades (ranging from 300 to 580 kg/m^3) were first performed to determine flexural tensile strength and fracture energy. Knowing that the mechanical parameters of quasi-brittle materials depend on the specimen size (so-called size-effect, [36]), the specimen dimensions were chosen according to the specifications of the relevant Standards. The dependency of material microstructure, as well as of total pore volume and pore distribution from density was investigated through X-Ray Diffraction (XRD) analysis, image analysis on thin sections and mercury intrusion porosimetry (MIP), respectively. Experimental results were finally analyzed and used for the calibration of a bi-linear cohesive law for AAC by adopting a neural network algorithm and interfacing Matlab code [37,38] with ABAQUS FE package [39].

2. Materials and methods

All the specimens were obtained from commercially available AAC blocks belonging to four density grades, i.e. $\rho = 300$, 350, 480, and 580 kg/m^3, respectively indicated as D1, D2, D3 and D4 in the next Sections. The blocks were produced in Italy at the production plant of the Manufacturer starting from the following raw materials: cement, lime, water, gypsum, siliceous sand, and a variable amount of aluminum as expanding agent (the quantity of aluminum was indeed varied to obtain different densities of the final product). Autoclaving of AAC green cake lasted approximately 11 h and was carried out with a system working at high temperature and pressure (about 180 °C and 12 bars). After the production process, the blocks (with dimensions equal to 600 × 250 × 300 mm^3) were directly cut at the production plant, and the specimens were then sent to the Laboratory of Materials and Structures of the University of Parma (Department of Engineering and Architecture) for the execution of material characterization tests. The adopted sampling scheme is deeper discussed in [4]. Shortly, from a single block, 3 + 3 twin cubes with 100 mm side were extracted to determine compressive strength and oven-dry density, together with 3 prismatic samples, having dimensions of 50 mm × 50 mm × 200 mm, for the determination of flexural tensile strength (series 1). From another twin block, one more prismatic sample with dimensions 50 mm × 50 mm × 200 mm was extracted to determine fracture energy, together with two cubes with 100 mm side for the control of compressive strength and oven-dry density; in this case all the specimens were only cut from the central part of the block (series 2). A general view of the adopted sampling scheme is shown in Fig. 1. For both series 1 and 2, this sampling scheme was repeated on 6 blocks for each investigated density. According to the European Standards EN 772–1 and EN1351 [40,41], before testing specimens were preliminary dried in a ventilated oven until the reaching of 6 ± 2% moisture content. After the execution of mechanical tests, one specimen for each density grade was sent to the Laboratory of the Department of Chemistry, Life Sciences and Environmental Sustainability of the University of Parma, to extract thin sections dedicated to image analysis and MIP, and powders for XRD.

2.1. Microstructural characterization and analysis of the porous structure of AAC

2.1.1. Mineralogical characterization via XRD analysis

Mineralogical analyses of AAC were performed with X-ray powder diffraction technique applied to sample powders. Before the analyses, AAC samples having different densities were oven-dried at 40 °C for two days, and subsequently small sample amounts (~0.5 g) were crushed into a jade mortar to reach an average grain size < 63 μm. Sample grain size reduction by milling is needed to avoid any diffraction and scattering of incident radiation during X-ray analysis due to the presence of coarse particles. Fine-grained powders were analyzed with a Bruker D2 PHASER X-ray diffractometer. Measurements of intensity peaks were performed at electric current values of 30 kV and 10 mA, adopting a CuKα radiation with a wavelength of 1.54060 Å. A 2θ scattering angle interval spanning from 6° to 60° was covered with progressive incremental steps of 0.02° at a constant counting time of 2 s for each step.

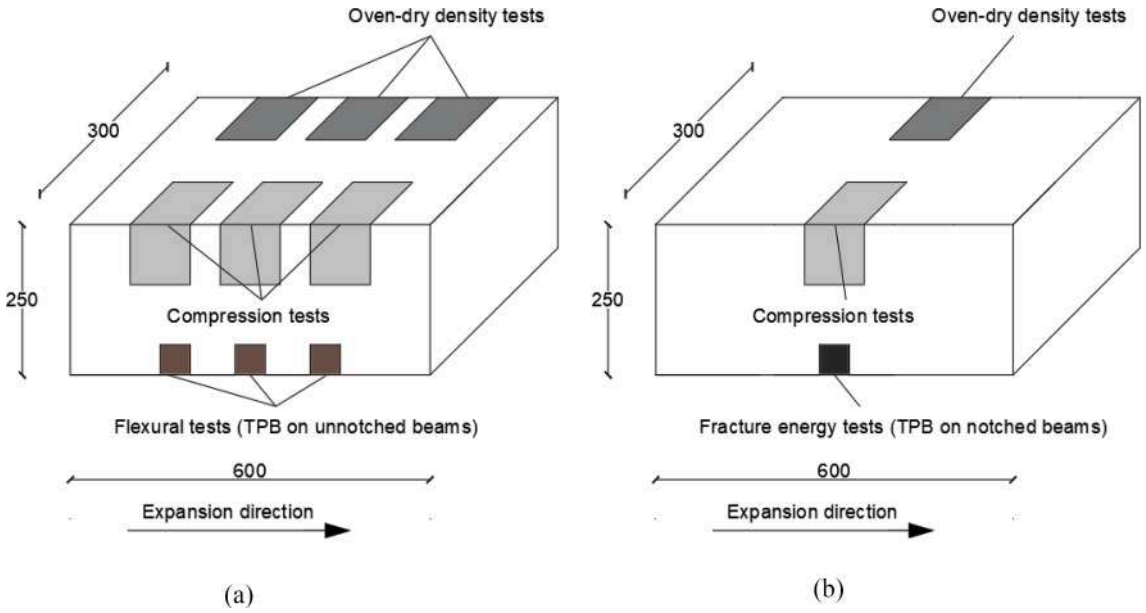

Fig. 1. General view of the adopted sampling scheme: (a) series 1, (b) series 2.

2.1.2. Bulk porosity estimation through 2D image analysis

AAC samples were cut to obtain petrographic thin section (~30 μm-thick), which were subsequently manually polished with a fine-grained (~1 μm) corundum abrasive powder. Before being cut, all samples were impregnated in Araldite epoxy resin to facilitate precise cutting due to the high fragility of AAC specimens. The epoxy resin was mixed with a blue dye to ease porosity recognition and calculation. High-resolution scans of whole thin section area were acquired with a Nikon Super-Cool Scan 5000. For each AAC sample, a total of 10 detail photomicrographs under 12.5 × magnification was acquired with a Zeiss Axioplan 2 petrographic microscope, equipped with a Leica MC 170 HD high-resolution camera. Image resolution was kept constant at 2592 × 1944 px. Acquired images were processed with ImageJ open-source image analysis software, to remove noise, outlier color pixel, and to slightly enhance the color contrast between pores and matrix. Blue-dyed pores with equivalent diameters > 200 μm were detected using semi-automatic color threshold identification technique. Manual correction of automatically traced pores was needed to increase the precision in identifying the correct pore boundary. Bulk porosity, mainly imparted by relatively coarse pores (>200 μm in diameter) was calculated by the ratio of the area associated to pores and the total area of the image. Results concerning bulk porosity of each AAC specimen are provided as an average value gained from 10 images, with the associated standard deviation.

2.1.3. Pore size distribution via mercury intrusion porosimetry (MIP)

Pore size distribution was obtained through mercury intrusion porosimetry, using a PoreMaster 33 porosimeter (Quantachrome Instruments). Before measurements, all 4 samples were dried at the controlled temperature of 40 °C for two days, and then small sample amounts (0.1–0.2 g) were carefully cut and analyzed. The instrument was equipped with a 1.0 × 3.0 cm analysis cell and the mercury pressure varied in the 0.5–33000 psi range. The porosimeter pore size analytical range was comprised between 0.0064–250 μm, with mercury contact angle equal to 140° and a mercury tension surface of 0.48 N/m. Porosimetry via mercury intrusion technique calculates the volume of mercury penetrating the sample at increasing applied hydraulic pressure. At low mercury pressure, only coarse pores are reached, while at higher pressure values, finer pores are properly measured. Following this, the total mercury intruded volume can be interpreted in terms of pore size distribution using the Washburn's equation [42]:

$$R = \frac{2\gamma \cos\theta}{p} \tag{1}$$

where R stands for the pore-throat radius that can be measured by the injected mercury, γ is the tension surface of liquid mercury, θ is the contact angle between mercury and the analyzed material and p is the applied hydraulic pressure.

2.2. Mechanical characterization of AAC specimens

Oven-dry density was determined according to EN 772-13 [43]. Cubic samples were dried in a ventilated oven at a temperature of 105 ± 5 °C until the reaching of constant mass. Oven-dry density was then calculated as the ratio between the oven-dried mass and the cube volume.

Compression tests were carried out following EN 772-1 [40], by using an Instron 5882 universal testing machine working with a loading rate of 0.05 MPa/s. Compressive strength was calculated as the ratio between the ultimate load and the area of the loaded surface.

For series 1, both compressive strength and oven-dry density of a single sample were calculated as the average value of three cubes, according to the sampling scheme reported in Fig. 1a, while for series 2, they were simply determined on a single cube according to Fig. 1b. For series 1 and 2, the mean values referred to a specific density grade were calculated as the average of 6 samples and 3 samples, respectively.

Flexural tests on un-notched beams were performed according to [41] by using an Instron 8862 universal testing machine working with a loading rate of 10 N/s. A TPB scheme was adopted, over a net span of 150 mm. Flexural tensile strength was then calculated as:

$$f_{t,fl} = \frac{1.5\ P\ell}{b_{fr}\ h_{fr}^2} \tag{2}$$

where P is the failure load, ℓ is the net span, b_{fr} and h_{fr} are the specimen dimensions in correspondence of the cracked section. The flexural tensile strength of each sample was calculated as the average of three prisms according to the sampling scheme of Fig. 1a, while the average flexural tensile strength for each density grade was the average of 6 samples. As already stated, before executing compression and flexural tests, the specimens were conditioned at a moisture content equal to 6 ± 2%, according to the relevant Standards [40,41].

The complete description of the followed test procedures is presented in [4], to which reference is made.

2.3. Experimental determination of fracture energy: three-point bending tests

Fracture energy was determined according to [34]. The same specimen geometry and loading arrangement adopted for flexural tests was used, but in this case a notch was cut in the central part of the specimen, with a notch depth approximately equal to 0.3 times the beam depth. A clip-gauge was fixed to the mouth of the notch and the tests were performed under CMOD control (Fig. 2), with a strain rate of 1 μm/min. Three beams were tested for each density grade, and all the samples were preliminarily conditioned at a moisture content of 6 ± 2% before testing. The evolution of midspan deflection with increasing loading was monitored through DIC technique, by continuously acquiring images of the specimen during the test, at a constant time interval of 5 s. For image acquisition, a Nikon D5100 camera placed on a stiff frame was used. One side of the specimen was preliminarily spray-painted, so to realize a speckle pattern formed by randomly distributed black dots over a white background (Fig. 2a, b), and was illuminated during test execution by means of a professional lamp. Displacement and strain fields were then obtained by using the software Ncorr [44]. The ratio of specimen height to the corresponding number of pixels was approximately 0.29 mm/px. Before analysing the images, the effect of subset radius and subset spacing on the standard deviation of the displacements was investigated according to [45,46]. The analysis revealed an optimal subset radius of 50 px and a subset spacing of 5 px. Strains were calculated by interpolating the displacements with a plane using a strain radius of 3 px. To verify the effectiveness of the followed procedure, the specimens were also equipped with a LVDT, mounted on the opposite side (not subjected to DIC), on a specific device fixed onto supports.

Fracture energy was then calculated by following the two different approaches presented in the Introduction, i.e. based on the area under the load-CMOD curve (approach 1, Eq. (3)), and based on the area under the load-midspan deflection curve (approach 2, Eq. (4)). In the first case, the following relation [34] was adopted:

$$G_{F,\,CMOD} = \frac{0.75\ W_0 + W_1}{A_{lig}} \tag{3}$$

with the following meaning of symbols: W_0 is the area below load-CMOD curve up to specimen failure, W_1 is the work done by the specimen deadweight and by that of the loading apparatus, and A_{lig} the ligament area (equal to $b \times h^*$, where h^* is the difference between the height of the specimen and that of the notch). For sake of clarity, symbols are also shown in Fig. 2c, d.

Based on approach 2, fracture energy was instead calculated as [47]:

$$G_F = \frac{\widetilde{W}_0 + mg\delta_0}{A_{lig}} \tag{4}$$

with the following meaning of symbols: $\widetilde{W}_0$ is the area under the load-midspan deflection curve; $m = m_1 + 2\ m_2$ is the sum of the mass of the beam portion within the supports and that of the loading apparatus directly weighting down on it; g is the acceleration due to gravity; and δ_0 is the midspan deflection at the instant when $P = 0$ and the beam breaks into two parts. A view of the fractured specimen is shown in Fig. 2b. It can be seen that fracture surfaces are almost plane, even if crack propagation is influenced by pore distribution within the material.

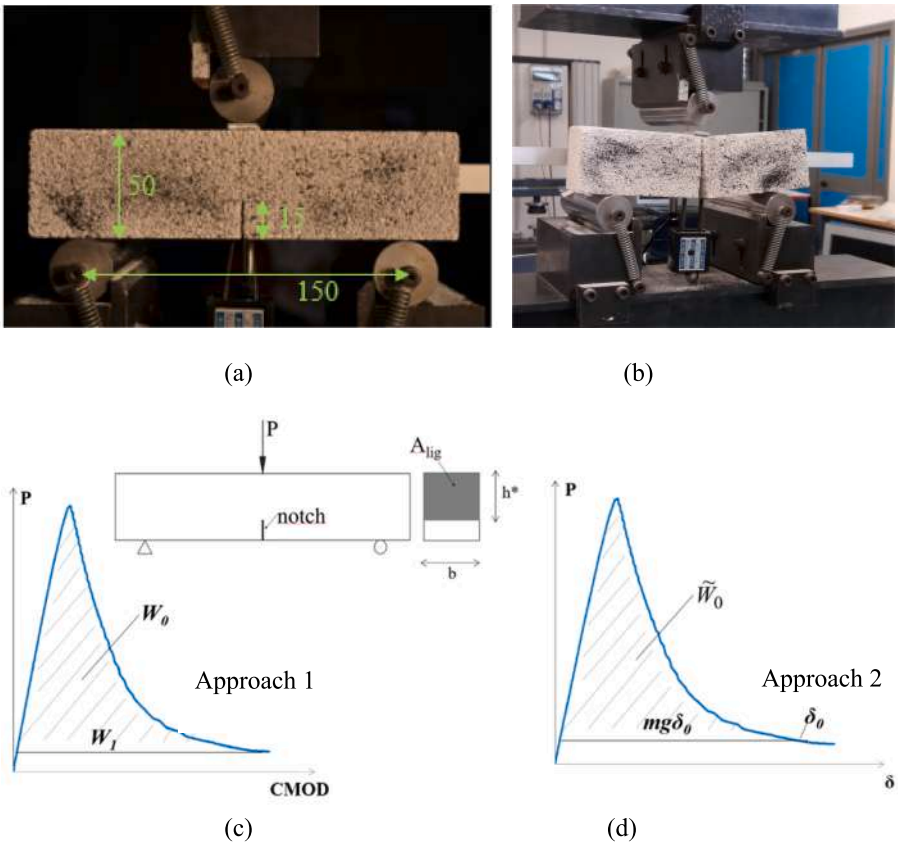

Fig. 2. (a) Test setup for the determination of fracture energy (dimensions in mm); (b) fractured specimen; sketch of the procedure followed to determine fracture energy according to approaches 1 (c) and 2 (d).

3. Results and discussion

3.1. Relation between porous structure and density

3.1.1. Mineralogical composition of AAC samples

As can be expected, all the four tested AAC samples D1-D4 showed almost equal X ray diffraction patterns despite their different density, with the same peaks (at same 2θ angles) and slight differences in count intensity (peak height), as shown in Fig. 3a. Detailed semi-quantitative analysis was carried out on D3 sample (with nominal density 480 ± 50 kg/m^3) to unravel the major and minor mineralogical phases (Fig. 3b). The most abundant mineralogical phases composing AAC specimens are quartz (SiO_2), hydrated Ca silicates (tobermorite, comprising silicates with formula varying from $Ca_4Si_6O_{15}(OH)_2{\cdot}5H_2O$ - $Ca_5Si_6O_{17}{\cdot}5H_2O$), calcite ($CaCO_3$), anhydrite ($CaSO_4$) and feldspar ($(Ca, Na, K)(Al, Si)_4O_8$), [48]. Minor mineralogical phases comprise Ca silicates (Ca_2SiO_4 - Ca_3SiO_5) and dolomite ($CaMg(CO_3)_2$) (Fig. 3b).

3.1.2. Bulk AAC porosity calculation from thin section image analysis

Bulk porosity estimation was performed through image analysis on photomicrographs, therefore, only pores with equivalent diameter > 150–200 μm were considered (Fig. 4). All macro-pores display an almost perfect circular shape, and their size is uniform in samples D1 and D2, while D3 and D4 are characterized by pores having different equivalent diameters (Fig. 4). Some of the pores are interconnected and a few of them were enlarged during sample cutting and successive resin impregnation, therefore they were neglected during porosity calculation (Fig. 5). A summary of bulk 2D porosity is reported in Table 1. According to density variation from sample D1 to sample D4, mean porosity displays a decrease from sample D1 (71.52%) to sample D4, which shows the lowest value (53.99%). Porosity calculated for D2 and D3 specimens falls in between, with mean values of 69.12% and 56.93%, respectively. The obtained results on macroporosity are in good agreement with those reported in [49]. From Fig. 6, it can be seen that the relation between the mean porosity determined though thin section image analysis and the density of the examined samples is almost linear.

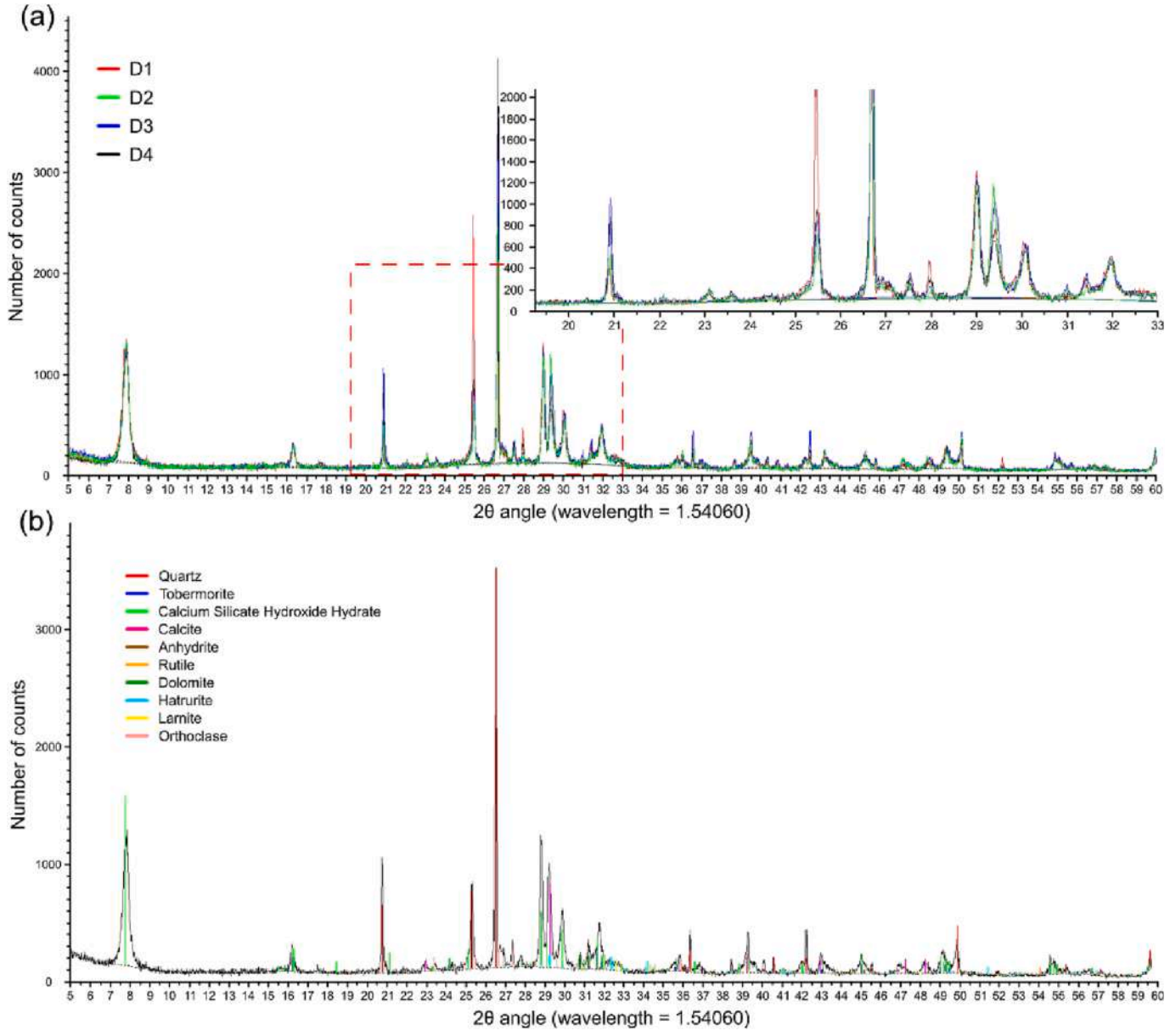

Fig. 3. Semi-quantitative XRD analysis diffractograms: (a) comparison of the results obtained for the 4 different specimens D1-D4; (b) semi-quantitative mineralogical phase identification carried out on D3 sample.

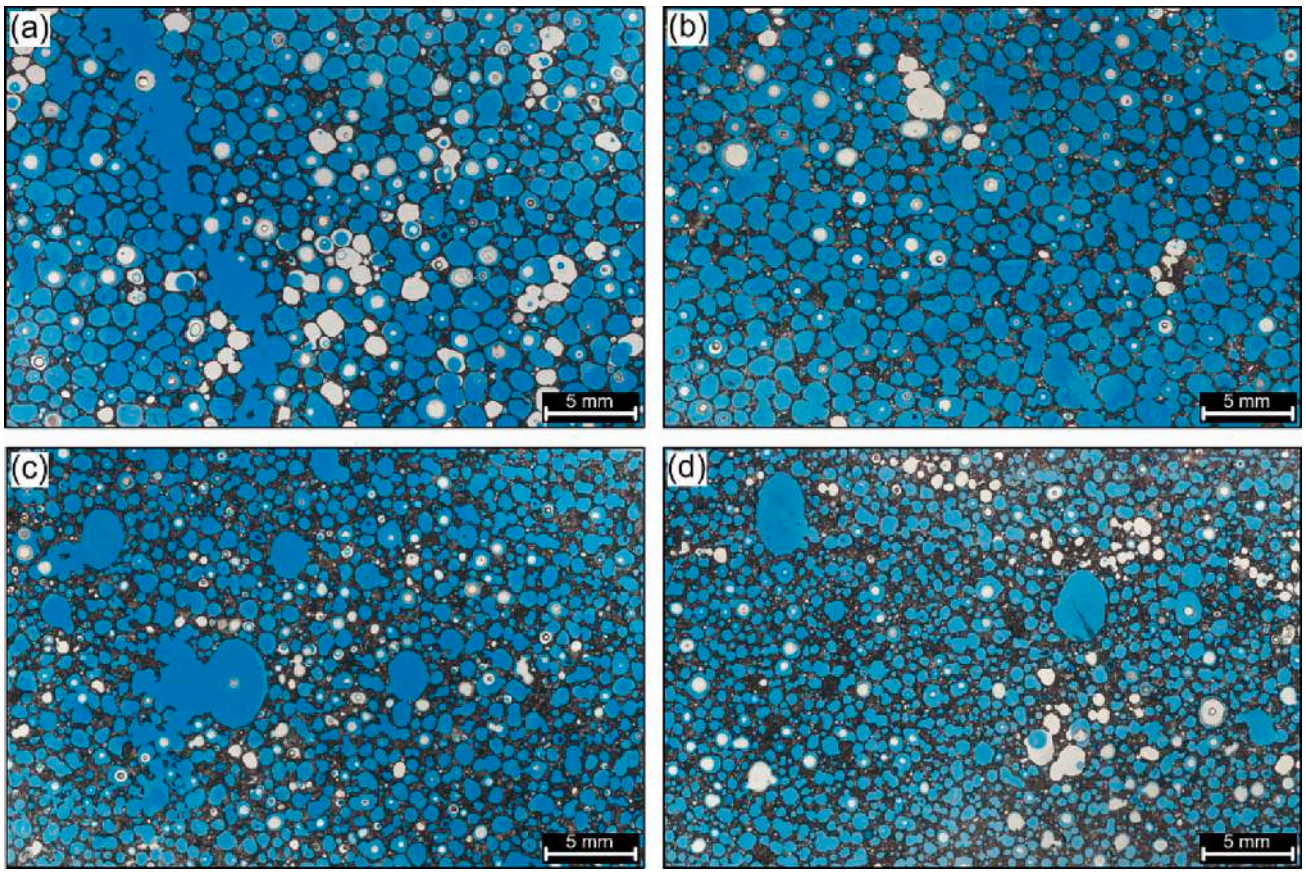

Fig. 4. High-resolution scans of blue-dyed thin sections displaying the porosity distribution and pattern: (a) sample D1; (b) sample D2; (c) sample D3; and (d) sample D4. (For interpretation of the references to color in this figure legend, the reader is referred to the web version of this article.)

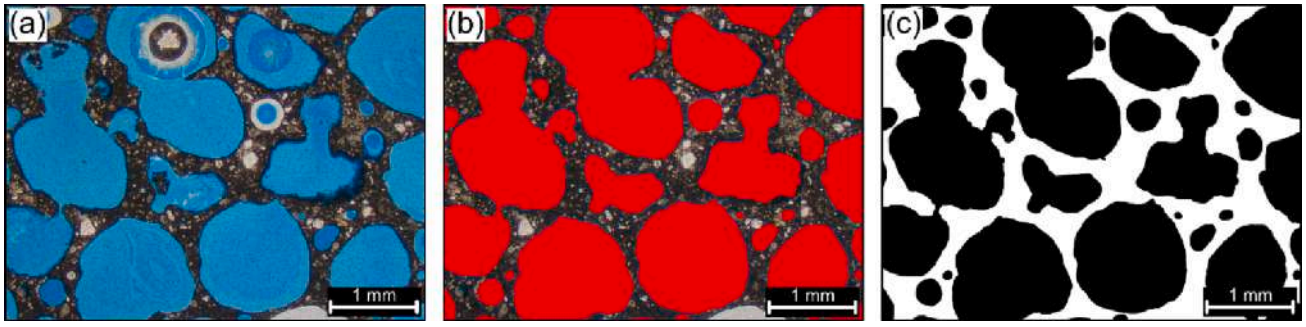

Fig. 5. Example of 2D porosity calculation via image analysis of detailed photomicrographs acquired under optical microscope: (a) blue-dyed original image; (b) color threshold applied to pore areas, manually corrected, and modified; (c) binary (black and white) image used to perform the porosity estimate. (For interpretation of the references to color in this figure legend, the reader is referred to the web version of this article.)

Table 1
Summary of 2D porosity estimation performed through image analysis from thin sections.

Specimen ID	Density (kg/m^3)	Mean 2D porosity (%)	Standard deviation (%)	Number of images
D1	300 ± 50	71.52	3.68	10
D2	350 ± 50	69.16	3.77	10
D3	480 ± 50	56.93	2.91	10
D4	580 ± 50	53.99	3.11	10

3.1.3. Pore size distribution (MIP)

MIP analyses performed on AAC samples provided the pore size distribution of pores with diameters comprised in the range 0.006–250 μm. Despite MIP is one of the most common techniques to determine pore size distribution in AAC, it should be reminded that most of the air pores cannot be detected, and that MIP may result in wrong pore sizes for inkbottle pores and bottle neck pore structures [50].

Despite their density, all the investigated specimens show characteristic bimodal pore diameter distributions, with a maximum in the microporous range, and another one in the macroporous range (as also found in [50–52]). Sample D1 has relative modal peaks at 0.25 and 140 μm, with a gap from 5 to 50 μm where no pores were measured (Fig. 7a). D2 sample has a continuous pore size distribution curve (without gaps), with relative maxima at 0.2–0-3 and 120 μm (Fig. 7b). D3 specimen is characterized by a pore size distribution separated in two by an interval from 12 to 40 μm where no pores were detected. Relative maxima are located at 0.18 and 100 μm (Fig. 7c). Eventually, sample D4 displays a

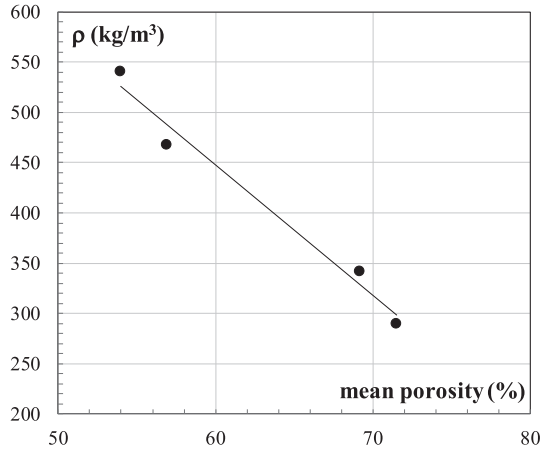

Fig. 6. Relation between density and mean porosity as determined from thin section image analysis.

continuous pore size curve with modal peaks at 0.15 and 50–60 μm (Fig. 7d).

3.2. Effect of density on the main AAC mechanical properties

The main mechanical properties obtained for series 1 samples, their dependency from density, and experimental failure modes were already discussed in another published work [4], to which reference is made for all the necessary clarifications. The main results are briefly summarized herein in Table 2, where they are also compared to the corresponding properties determined from series 2 samples, which were used for the determination of fracture energy as discussed in Section 3.3.

It can be seen that the differences between the average oven-dry density values as determined on 6 samples of series 1 (3 cubes for each sample) and on 3 samples of series 2 (only one central cube for each sample) ranges between 1% and 8%. Similar differences were also found for the average compressive strength, even if a larger value, almost equal to 18%, was registered for a density grade of 580 kg/m^3. This is not surprising due to the limited number of samples tested in series 2; for that reason, a higher coefficient of variation was found and the average strength was much more influenced from the extreme values.

Based on the experimental results obtained for series 1 samples, the following best-fitting equations (exponential and linear) relating compressive strength with density were deduced:

$$f_c = a_1 e^{b_1 \rho} \left(R^2 = 0.96\right) \tag{5}$$

with a_1 = 0.7375 (0.6024, 0.8726) and b_1 = 0.0034 (0.0030, 0.0037), where the values in bracket give the 95% confidence interval of the coefficients;

$$f_c = c_1 \rho + d_1 \left(R^2 = 0.94\right) \tag{6}$$

with c_1 = 0.01144 (0.01019, 0.01269) and d_1 = -1.482 (-2.045, -0.9185), and being ρ in kg/m^3, and f_c in MPa.

Table 2
Properties of AAC specimens for different density grades, with (6 ± 2) % moisture content (the Coefficient of Variation CV of the results is reported in brackets).

Density (kg/m^3)	Oven-dry density – series 1 (kg/m^3)	Compressive strength – series 1 (MPa)	Oven-dry density – series 2 (kg/m^3)	Compressive strength – series 2 (MPa)	Flexural tensile strength (MPa)
300 ± 50	295 (0.007)	1.93 (0.04)	290 (0.003)	1.91 (0.07)	0.65 (0.13)
350 ± 50	346 (0.008)	2.56 (0.03)	342 (0.003)	2.29 (0.03)	0.77 (0.08)
480 ± 50	506 (0.002)	3.94 (0.08)	468 (0.002)	3.80 (0.06)	1.13 (0.05)
580 ± 50	588 (0.005)	5.49 (0.08)	541 (0.007)	4.67 (0.11)	1.44 (0.05)

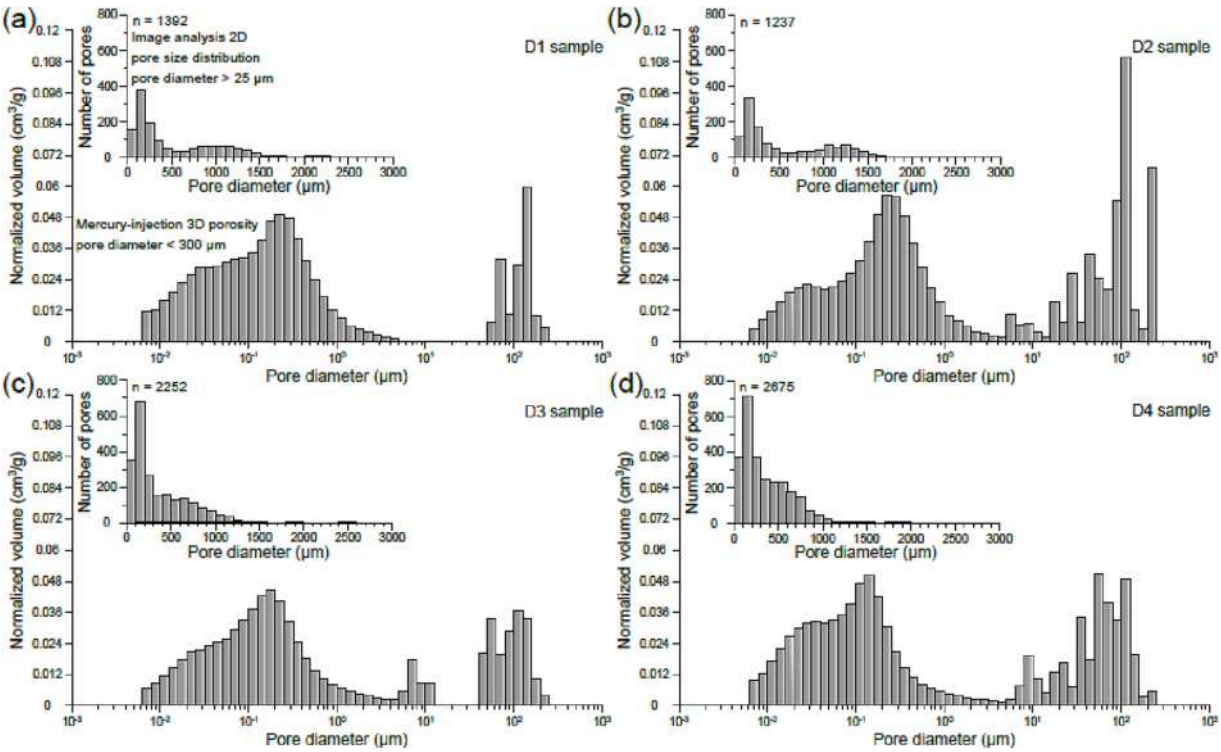

Fig. 7. Pore size distribution obtained from MIP analysis on AAC prepared samples: (a) sample D1; (b) sample D2; (c) sample D3; and (d) sample D4.

The best fitting equations relating flexural tensile strength and density were:

$$f_{t,fl} = a_2 e^{b_2 \rho} \quad (R^2 = 0.96) \tag{7}$$

with $a_2 = 0.2954$ (0.2558,0.3349) and $b_2 = 0.0027$ (0.002437,0.00296);

$$f_{t,fl} = c_2 \rho + d_2 \quad (R^2 = 0.95) \tag{8}$$

with $c_2 = 0.0027$ (0.0024,0.00292) and $d_2 = -0.1495$ (-0.2712, −0.02775), being ρ in kg/m^3, and $f_{t,fl}$ in MPa.

Based on the reported values of R^2, it can be seen that the dependency of compressive and flexural tensile strength from density can be represented with a quite similar degree of approximation with both the linear and exponential relations. Therefore, it is reasonably to infer that also the dependency of direct tensile strength from density might be almost linear.

Direct tensile strength was deduced in this work by exploiting the results of DIC relative to the samples belonging to series 2, and elaborating the so obtained data by means of inverse Finite Element (FE) analysis, as better discussed in Section 4. As a first step, the initial cracking load P_{cr} and the peak load P were determined from the analysis of DIC images for all the tested specimens, and the ratio P_{cr}/P was calculated. As an example, Fig. 8a,b show the map of horizontal strains at peak load and in the softening branch ($P/P_{max} = 0.46$) respectively for specimen D4-1. Fig. 8b also shows the extent of the Fracture Process Zone (FPZ) calculated from the gradient of the horizontal displacements, following the procedure described in [45,46].

According to Table 3, it can be observed that the ratio P_{cr}/P is almost independent from density and stands at a value approximately equal to 0.53. Direct tensile strength f_t was then derived from inverse FE analysis, by determining the tensile stress at the notch tip for an applied load equal to the experimental cracking load obtained from DIC. As reported in Table 3, also the ratio $f_t / f_{t,fl}$ is almost constant, ranging between 0.54 and 0.57 for all the investigated densities. These values are quite in line with those reported in [53], which are comprised between 0.56 and 0.68. Therefore, the best fitting equation relating direct tensile strength f_t coming from the elaborated data with density was:

$$f_t = 0.0016\rho - 0.1206 \quad (R^2 = 0.99) \tag{9}$$

3.3. Effect of density on AAC fracture energy

The main results of fracture energy tests are summarized in Table 4, where G_F is reported as a function of material density for a reference moisture content of 6%. As can be seen, midspan deflection was deduced by means of DIC for all the specimens (except for specimen D2-2, due to acquisition problems during the test), while LVDT measurements – which served as controls – were only performed for a couple of specimens for each density grade. The deflection measurements performed with the two techniques (LVDT vs. DIC) showed a generally good agreement, both in terms of averages values (see Table 4) and in terms of applied load P vs. mispan deflection δ curve (as an example see Fig. 9, which is referred to the lower density grade specimens, D1). For this reason, further comparisons involving the evaluation of fracture energy according to approach 2 are only made with reference to DIC results.

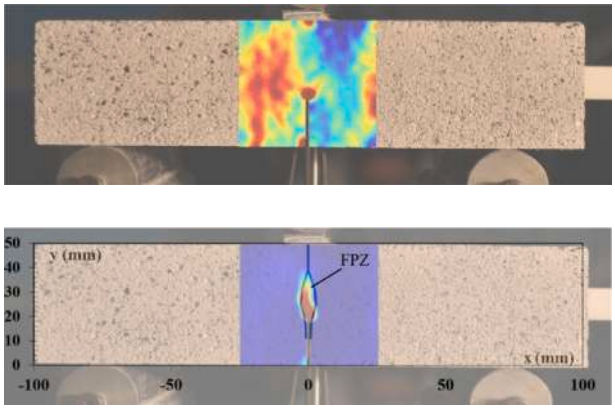

Fig. 8. Horizontal strain field obtained from DIC (Specimen D4-1): (a) at peak load; (b) in the softening branch ($P/P_{max} = 0.46$).

The experimental applied load P vs. CMOD curves and applied load P vs. midspan deflection δ (as obtained from DIC) curves for different density grades are summarized in Fig. 10. It can be observed that the curves are influenced by material density (and therefore by the compressive strength), as higher density specimens are characterised by higher peak load values as well as greater displacements/CMOD. A good agreement can be noted also in this case between the two families of graphs, if we take in mind that the area under the load – CMOD curve is greater than that under the load–deflection curve, and should be therefore reduced through a factor equal to 0.75 according to [34].

The dependency of fracture energy from density is plotted in Fig. 11a, reporting both the results obtained from approach 1 and 2, with the relative best-fitting linear equations, that are expressed in the form:

$$G_F = a\rho + b \tag{10}$$

with $a = 0.0135$ (0.0098, 0.0172) and $b = -1.83$ (-3.379, -0.2742) for approach 1, and $a = 0.01471$ (0.01081, 0.01861) and $b = -2.396$ (-4.051, -0.7401) for approach 2, where the values in bracket give the 95% confidence interval of the coefficients. In deriving the best-fitting equations, the anomalous point relative to specimen D3-1 (which is however reported in the graph of Fig. 11) was discarded. In any case, the poor R^2 value and the large confidence intervals are due to the unavoidable scatter of the experimental points, and can only be reduced by increasing the number of experimental tests for each density value. The dependency of fracture energy G_F from compressive strength f_c is instead shown in Fig. 11b.

4. Calibration of a cohesive model through a neural network algorithm

4.1. Finite element model

The cohesive law was calibrated through inverse analysis by modeling the three-point-bending tests using the finite element software Abaqus [39]. Specifically, the specimen was modeled in plane stress conditions using about 7000 four-node plane stress elements (element type CPS4R) of size 1.2 mm × 1.2 mm (Fig. 12). The supports and load rollers were modeled as rigid parts. The interface between specimen and rollers was simulated using Coulomb's friction law (with friction coefficient 0.4). The analysis was carried out by applying a force that was varied using the Riks' method.

The mechanical behavior of AAC was modelled using the "Concrete Damage Plasticity'' CDP model [54], a continuum model based on plasticity and damage with distinct failure surfaces for tensile cracking and compressive crushing. Since a specific calibration of CDP parameters for AAC is not available in the literature, the standard parameters for concrete were adopted [55] in this study, as done also in other published works on AAC [28]. The triaxial behavior of CDP was then defined by the following four parameters: the ratio between biaxial and uniaxial compressive strength $f_{b0}/f_{c0} = 1.16$; the ratio between second stress invariant on the tension meridian and second stress invariant on compression meridian $K_c = 0.667$; the eccentricity of the plastic potential surface $e = 0.1$; and the dilation angle $\psi = 30°$. However, it should be noted that there is no agreement in the literature regarding the value to be assumed for the dilatation angle in case of AAC, with suggested values ranging between 20° and 30° [56–58]. Some Authors [59]

Table 3
Cracking and peak loads for the examined specimens as derived from DIC analysis, and direct tensile strength obtained from inverse FE analysis.

Density (kg/m³)	*Specimen ID*	*P_{cr} (kN)*	*P (kN)*	*P_{cr}/P (-)*	*P_{cr}/P (-) mean*	*f_t (MPa)*	*f_t / $f_{t,fl}$ (-)*
300 ± 50	D1-1	0.051	0.098	0.520	0.44	0.37	0.57
	D1-2	0.041	0.077	0.532			
	D1-3	0.023	0.083	0.277			
350 ± 50	D2-1	0.061	0.102	0.598	0.58	0.43	0.56
	D2-2	0.043	0.093	0.462			
	D2-3	0.062	0.091	0.681			
480 ± 50	D3-1	0.098	0.177	0.554	0.56	0.61	0.54
	D3-2	0.068	0.129	0.527			
	D3-3	0.082	0.135	0.607			
580 ± 50	D4-1	0.089	0.172	0.517	0.54	0.82	0.57
	D4-2	0.098	0.189	0.519			
	D4-3	0.111	0.194	0.573			

Table 4
Experimental values of fracture energy for different density grades, for a nominal moisture content of 6%.

Density (kg/m³)	*Specimen ID*	*$G_{F\ CMOD}$ (N/m)*	*$G_{F\ CMOD,\ mean}$ (N/m)*	*$G_{F\ LVDT}$ (N/m)*	*$G_{F\ LVDT,\ mean}$ (N/m)*	*$G_{F\ DIC}$(N/m)*	*$G_{F\ DIC,\ mean}$ (N/m)*
300 ± 50	D1-1	2.13	1.99	/	2.01	1.98	1.99
	D1-2	1.90		1.83		2.01	
	D1-3	1.94		2.19		1.98	
350 ± 50	D2-1	3.08	2.95	/	2.65	3.23	2.51
	D2-2	2.99		2.73		/	
	D2-3	2.78		2.56		1.78	
480 ± 50	D3-1	6.83	5.20	7.20	5.70	6.74	5.06
	D3-2	3.88		/		3.78	
	D3-3	4.88		4.19		4.67	
580 ± 50	D4-1	6.62	5.52	/	6.17	6.35	5.71
	D4-2	5.18		5.50		5.60	
	D4-3	4.76		6.84		5.18	

also suggest to apply a value of $\psi = 10°$, which is commonly adopted for simulating the behavior of traditional unreinforced masonry [60]. Despite its importance when modelling full scale elements, the value of the dilatation angle has a limited influence on the numerical analyses discussed in this paper, because in case of bending the compression zone has a very limited extension. The viscosity parameter, which improves the numerical stability of the iterative solution, was chosen as $\nu = 0.0002$. Compression behavior was described using the stress-plastic strain law σ-ε_{cp} shown in Fig. 13a, while the bilinear function shown in Fig. 13b was chosen for the cohesive law σ-w. The fracture is represented using the crack band model instead of cohesive elements, but the approach, as demonstrated in [61], is perfectly equivalent. Since a post-failure stress-displacement curve is adopted in this work, Abaqus transforms displacements into deformations by automatically dividing them by the characteristic length of the element, which depends on element geometry and formulation. In the present case, with elements of type CPS4R, the internal length is equal to the square root of the element area. The mesh was constructed with square elements aligned with the crack and of constant size to avoid the problems well highlighted by Jirasek and Bauer [62].

Relevant studies in the literature have shown that for quasi-brittle materials, the bilinear law is preferable to the linear and exponential laws because it allows the experimental load-CMOD curve to be better replicated [36]. The bilinear law is characterized by four parameters: the direct tensile strength f_t, the fracture energy of the first branch G_f, the stress that locates the knee σ_k, and the total fracture energy G_F (Fig. 13b). For specimens in the laboratory scale, the first two parameters govern the peak of the load-CMOD curve, while the last two govern its softening branch [36]. Some researchers measure tensile strength by splitting or direct tensile tests, although these quantities may be affected by a size-effect [36]. Some others prefer to define the tensile strength f_t by observing by laser interferometry the crack onset [26,63]. Also DIC can also be used for the purpose, although it is not as accurate [46,64]. Because of its simplicity, DIC was used in this work; specifically, the cracking load was determined by looking at the onset of jumps in the horizontal displacements in DIC images. Then, the tensile strength f_t was

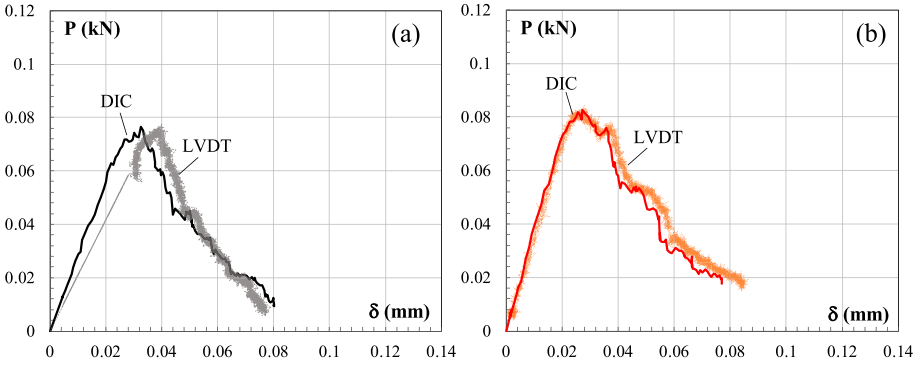

Fig. 9. Comparison between the results obtained from DIC and LVDT measurments, in terms of load P vs. midspan deflection δ, for specimens (a) D1-2 and (b) D1-3 with a nominal density grade of 300 ± 50 kg/m³.

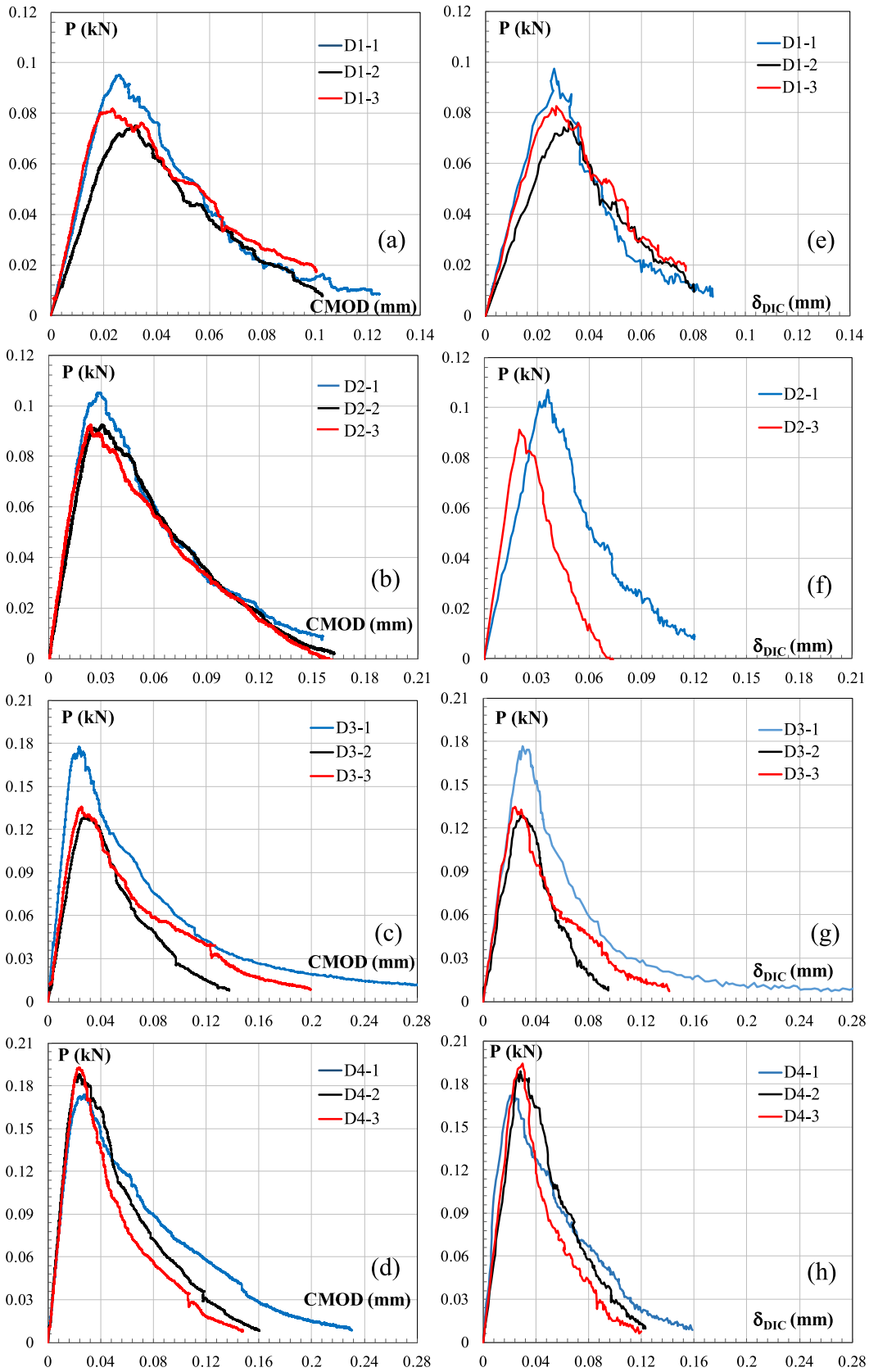

Fig. 10. Experimental results of TBP tests on notched beams with different densities in terms of: (a)-(d) applied load *P* vs. CMOD; (e)-(h) applied load P vs. midspan deflection δ (for specimen nomenclature refer to Table 4).

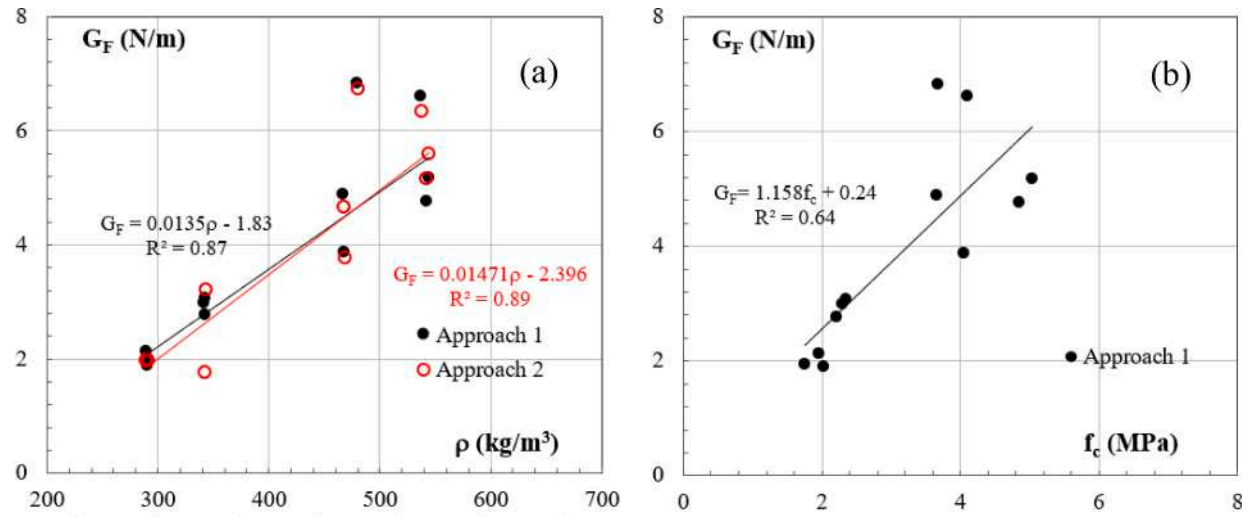

Fig. 11. Experimental dependency of fracture energy from (a) density, according to approaches 1 and 2; (b) compressive strength, according to approach 1.

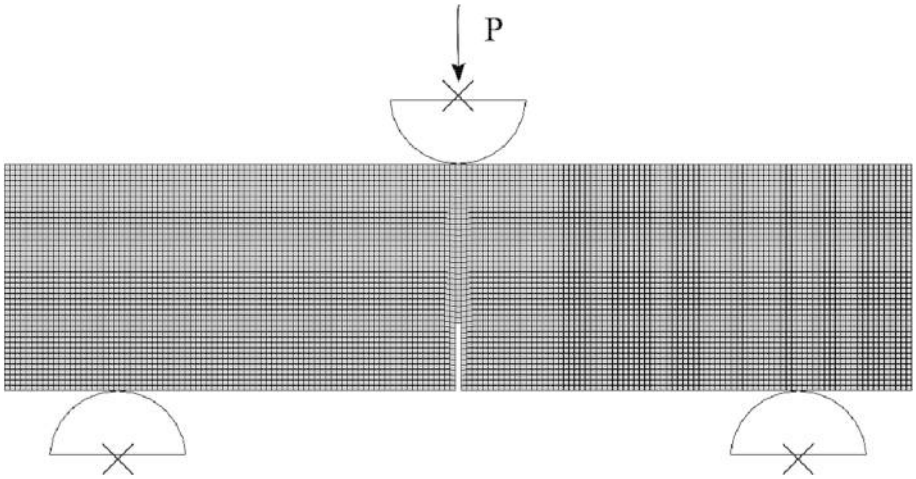

Fig. 12. Finite element model of the TPB test.

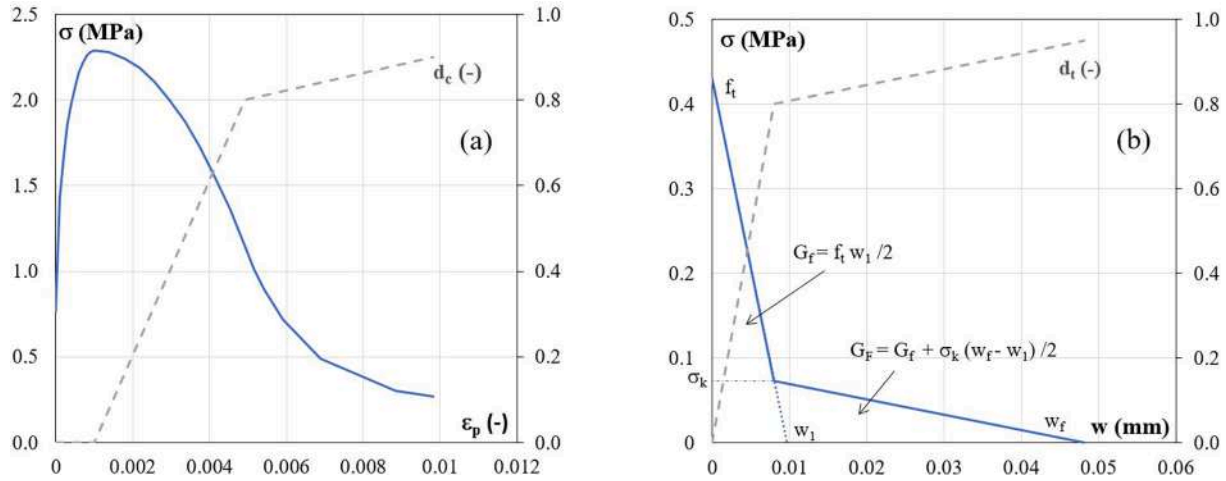

Fig. 13. Concrete damage-plasticity model: (a) Compression behavior; (b) Cohesive law, for specimens of density D2.

fixed and taken equal to the stress at the crack tip of the FE model in correspondence of the cracking load. The Young modulus *E* of the material was determined by imposing that the experimental and the numerical curves were superimposed in the initial linear elastic branch. More specifically, the following values were assumed: 823 MPa, 1374 MPa, 1424 MPa, 1930 MPa for density ranging from D1 to D4, that are in

line with those experimentally determined in [4].

4.2. Adopted neural network algorithm

Cohesive law parameters $\boldsymbol{x} = [G_f, \sigma_k, G_F]$ were calibrated by fitting the experimental load-CMOD curve with that obtained from the finite element model previously discussed, through the minimum least-squares method. In more detail, the followed procedure consisted in minimizing the function:

$$S = \sum_{i=1}^{n} \left(F_{test}\left(CMOD_i\right) - F_{FEM}\left(\boldsymbol{x}, CMOD_i\right) \right)^2 \quad (11)$$

where $F_{test}(CMOD_i)$ are the experimental data, $F_{FEM}(\boldsymbol{x}, CMOD_i)$ are the data coming from the finite element model, $CMOD_i$ is the sampling value of CMOD, and n is the number of equally spaced points chosen to represent the curve (in the present study, $n = 50$).

The procedure requires evaluating the finite element curve $F_{FEM}(\boldsymbol{x}, CMOD)$ many times, to find the best set of the parameters $\boldsymbol{x}$ that allows obtaining a solution that fits the average experimental curve, and therefore is particularly time-consuming. For this reason, the approach described in Papazafeiropoulos et al. [38] was used in the present work. Accordingly, F_{FEM} was replaced with F_{NET}, obtained by fitting with neural networks a number N of $F_{FEM,j}(\boldsymbol{x}_j, CMOD)$ curves plotted for different trial values of the unknown parameters $\boldsymbol{x}_j$. To span a possible range for the solution, nine trial values ($N = 9$) of vector $\boldsymbol{x}$ were chosen, by taking initial values and their variation ± 25%. This operation was performed using the Matlab app *Neural Network Fitting*. The network was composed of 10 hidden layers and was trained using the Bayesian Regularization Method [37]. Mean Squared Error (MSE) was used for the loss. Division of data for training, validation, and testing of the network was 80%, 15%, and 5% respectively.

After defining the neural network, Eq. (11) was used two times, one for the rising branch of the experimental curve to determine G_f (using trial values for σ_k and G_F), and the other for the softening branch to determine σ_k and G_F (using G_f previously computed), as suggested in [36]. To check the soundness of the best-fitted parameters, the corresponding F_{FEM} curve was calculated, and function S defined in Eq. (11) was evaluated. In order to define F_{FEM}, *Abaqus2matlab* [38] was used to interface Abaqus and Matlab, so allowing both to edit the model input file, and to read the results of the Abaqus simulations within the Matlab environment. The minimum of function S was searched with the Matlab function *fminsearch*, which is based on the Nelder-Mead simplex direct search method [65]. This method was chosen because it does not employ either numerical or analytical gradients, and theoretically requires less evaluation of the F_{FEM} function. If the minimum of S was attained with an error less than a predefined tolerance the procedure reached convergence and stopped; otherwise, the F_{FEM} curve was added to the $F_{FEM,j}$, then F_{NET} was recalculated through the neural network algorithm and the procedure was repeated iteratively. It usually required less than 10 iterations to reach an error $\varepsilon < 0.001$.

4.3. Derivation of cohesive law parameters as a function of density

The described procedure was applied to the mean experimental curves obtained for the 4 investigated densities. As an example, Fig. 14a shows the nine trial curves fitted by the Neural Network, and Fig. 14b reports the comparison between the numerical best fitted curve and the experimental ones relative to the specimen with density D4. Similar results were found also for densities D1-D3. Experimental and numerical results are in good agreement, so proving the ability of the bi-linear cohesive law to represent both the peak and the shape of the softening branch of the experimental curves.

The obtained cohesive laws are plotted in Fig. 15a for different block densities. The curves are characterized by a different maximum cohesive traction, corresponding to the tensile strength, while the displacements corresponding to the knee of the curve are almost superimposed. If the curves are plotted as a function of dimensionless stresses (i.e. cohesive traction divided by tensile strength), they appear to be substantially superimposed (Fig. 15b) considering the ineluctable experimental uncertainties. Looking at the curves, it is as if the stresses were scaled with porosity. The parameters defining the cohesive law f_t, σ_k/f_t, G_f, and G_F/G_f are given in Table 5 for the four density values. The value of the fracture energy reported in Table 5 is the one subtended by the cohesive law, $G_F = G_{F,FEM}$. The value of $G_{F,FEM}$ is slightly larger than that calculated from the experimental curve (Table 4), partly because the experimental curve did not reach the complete failure of the specimen.

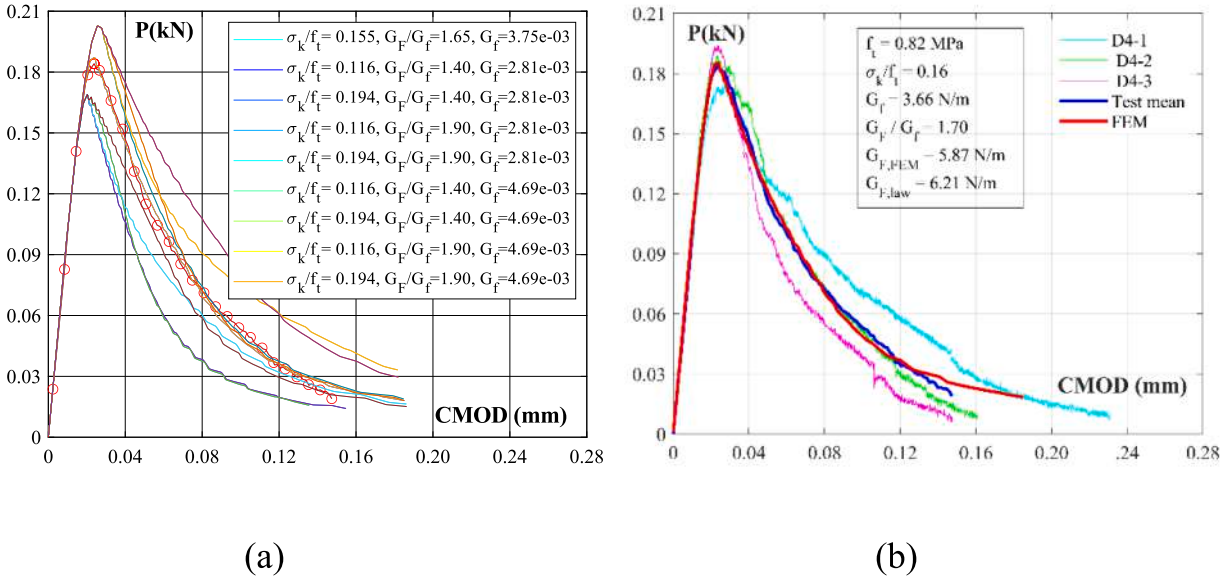

Fig. 14. Fitting of Load-CMOD curves for the specimens D4: (a) Trial curves to be fitted with neural networks; (b) Results of best fitting procedure.

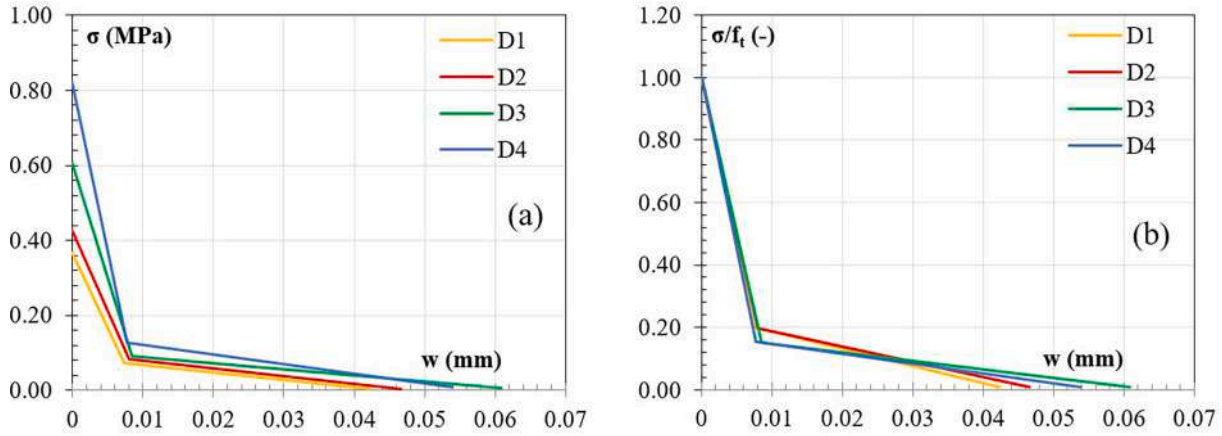

Fig. 15. (a) Proposed cohesive laws for different material densities; (b) Proposed cohesive laws with stress σ divided by tensile strength f_t.

Table 5
Parameters of the cohesive laws calibrated for different values of density.

Density (kg/m³)	*f_t (MPa)*	*G_f (N/m)*	*σ_k / f_t (-)*	*G_F / G_f (-)*	*G_F (N/m)*
300 ± 50	0.37	1.70	0.20	1.41	2.39
350 ± 50	0.43	2.13	0.20	1.65	3.52
480 ± 50	0.61	3.03	0.15	1.73	5.24
580 ± 50	0.82	3.66	0.16	1.70	6.21

5. Conclusions

This work experimentally investigates the dependency of AAC porous structure and mechanical properties from material density. Four material densities are analyzed, ranging from 300 kg/m^3 to 580 kg/m^3, corresponding to a compressive strength interval of 1.90–5.50 MPa. Variation of fracture energy with density was preliminary assessed through experimental tests. Then, a bi-linear cohesive law was calibrated for each density/strength, by exploiting a neural network algorithm and interfacing MatLab with ABAQUS Finite Element package. Based on the obtained results, the following conclusions can be drawn:

- since the material composition is the same for all AAC samples, and porosity is varied by changing the dosage of aluminum powder in the admixture, almost equal X-ray diffraction patterns are found regardless of specimen density. All the investigated specimens show characteristic bimodal pore diameter distributions, and the mean porosity (as derived from thin section image analysis) shows a linear dependence on density;
- the experimental dependence of mechanical parameters (compressive strength, flexural tensile strength, and fracture energy) on density can be reasonably represented by a linear relationship. The ratio of direct tensile strength (as derived from inverse FE analysis) to flexural tensile strength is almost constant, ranging from 0.54 to 0.57 for all the investigated densities;
- the two approaches for the determination of the fracture energy, based respectively on the evaluation of the area under the load-CMOD curve, properly reduced by a factor equal to 0.75, and on the evaluation of the area under the load–deflection curve obtained from TPB tests on notched beams, give very similar results; for the range of densities studied, G_F varies approximately between 1.99 and 5.52 N/m.
- cohesive laws for different densitiesare obtained from numerical analysis and calibrated on experimental results. The curves are characterized by a different maximum cohesive traction, corresponding to the tensile strength, which varies between 0.37 and 0.82 MPa, while the displacements corresponding to the knee of the curve are almost superimposed, which seems indicating that fracture mechanism is independent from material density. When the curves are plotted as a function of dimensionless stresses (i.e. cohesive traction normalized with respect to material tensile strength), they appear to be substantially superimposed to each other as if the stresses were scaled with porosity.

The obtained cohesive laws, together with the other mechanical parameters, can be proficiently used to carry out numerical simulations not only of AAC structural elements, but also of AAC infills in framed structures, providing a realistic representation of their cracking behavior. Further studies are required to deepen the knowledge of micromechanics governing crack onset and propagation, as well as the dependence of fracture energy on specimen size.

CRediT authorship contribution statement

E. Michelini: Conceptualization, Data curation, Formal analysis, Investigation, Methodology, Supervision, Validation, Writing – original draft, Writing – review & editing. **D. Ferretti:** Conceptualization, Data curation, Formal analysis, Funding acquisition, Investigation, Methodology, Project administration, Software, Supervision, Validation, Writing – review & editing. **M. Pizzati:** Data curation, Investigation, Writing – original draft.

Declaration of Competing Interest

The authors declare that they have no known competing financial interests or personal relationships that could have appeared to influence the work reported in this paper.

Data availability

Data will be made available on request.

Acknowledgements

The experimental part of this work was carried out within PON national project n. F/090017/00/X36, CUP B18I17000450008 assigned to Ekoru s.r.l. Authors gratefully thank Dr. F. Talento, Arch. A. Riva, L. Barchi and Dr. L. Mantovani for their valuable help.

References

[1] A.W. Hendry, Masonry walls: materials and construction, Constr. Build. Mater. 15 (2001) 323–330, https://doi.org/10.1016/S0950-0618(01)00019-8.
[2] F. Pacheco-Torgal, P.B. Lourenço, J.A. Labrincha, S. Kumar, P. Chindaprasirt (Eds.), Eco-efficient Masonry Bricks and Blocks - Design, Woodhead Publishing, Oxford, Properties and Durability, 2015.

[3] D. Ferretti, B. Gherri, E. Michelini, Eco-mechanical indexes for sustainability assessment of AAC blocks, in: IOP Conf. Ser. Mater. Sci. Eng., IOP Publishing, 2018, p. 12011.
[4] D. Ferretti, E. Michelini, The effect of density on the delicate balance between structural requirements and environmental issues for aac blocks: an experimental investigation, Sustainability. 13 (2021) 13186.
[5] C. Fudge, AAC - Providing sustainable building solutions, AAC Worldw. (2022).
[6] Transforming our world: the 2030 Agenda for Sustainable Development; accessible at: https://www.un.org/en/development/desa/population/migration/generalassembly/docs/globalcompact/A_RES_70_1_E.pdf.
[7] B. Rosti, A. Omidvar, N. Monghasemi, Optimal insulation thickness of common classic and modern exterior walls in different climate zones of Iran, J. Build. Eng. 27 (2020), 100954.
[8] M. Abdul Mujeebu, F. Bano, Integration of passive energy conservation measures in a detached residential building design in warm humid climate, Energy. 255 (2022) 124587.
[9] M. Vanheukelom, R. Das, H. Degée, B. Vandoren, Experimental characterization of the initial shear strength of composite masonry including AAC blocks and DPC layers, Sustainability. 13 (2021) 12749.
[10] H. Radhi, Viability of autoclaved aerated concrete walls for the residential sector in the United Arab Emirates, Energy Build. 43 (9) (2011) 2086–2092.
[11] A. Artino, G. Evola, G. Margani, E.M. Marino, Seismic and energy retrofit of apartment buildings through autoclaved aerated concrete (AAC) blocks infill walls, Sustainability. 11 (2019) 3939.
[12] A. Thakur, A.K. Tiwary, A Comparative Study on Conventional Clay Bricks and Autoclaved Aerated Concrete Blocks, in: IOP Conf. Ser. Earth Environ. Sci., IOP Publishing, 2021, p. 12061.
[13] D. Ferretti, E. Michelini, N. Pongiluppi, R. Cerioni, Damage assessment of autoclaved aerated concrete buildings: some Italian case studies, Int. J. Mason. Res. Innov. 5 (2) (2020) 279–301.
[14] T. He, R. Xu, Y. Da, R. Yang, C. Chen, Y. Liu, Experimental study of high-performance autoclaved aerated concrete produced with recycled wood fibre and rubber powder, J. Clean. Prod. 234 (2019) 559–567.
[15] Z. Li, L. Chen, Q. Fang, H. Hao, Y. Zhang, W. Chen, H. Xiang, Q. Bao, Study of autoclaved aerated concrete masonry walls under vented gas explosions, Eng. Struct. 141 (2017) 444–460.
[16] Z.O. Pehlivanlı, I. Uzun, Z.P. Yücel, I. Demir, The effect of different fiber reinforcement on the thermal and mechanical properties of autoclaved aerated concrete, Constr. Build. Mater. 112 (2016) 325–330.
[17] X. Qu, X. Zhao, Previous and present investigations on the components, microstructure and main properties of autoclaved aerated concrete–A review, Constr. Build. Mater. 135 (2017) 505–516.
[18] A. Raj, A.C. Borsaikia, U.S. Dixit, Finite Element Modeling of Autoclave Aerated Concrete (AAC) Masonry for Estimation of Strength, Manuf. Eng., Springer, 2020, pp. 511–524.
[19] A. Hillerborg, M. Modéer, P.-E. Petersson, Analysis of crack formation and crack growth in concrete by means of fracture mechanics and finite elements, Cem. Concr. Res. 6 (6) (1976) 773–781.
[20] G.I. Barenblatt, The mathematical theory of equilibrium cracks in brittle fracture, Adv. Appl. Mech. 7 (1962) 55–129.
[21] J.R. Rice, Mathematical analysis in the mechanics of fracture, Fract. an Adv. Treatise. 2 (1968) 191–311.
[22] F.H. Wittmann, I. Gheorghita, Fracture toughness of autoclaved aerated concrete, Cem. Concr. Res. 14 (3) (1984) 369–374.
[23] E. Brühwiler, J. Wang, F.H. Wittmann, Fracture of AAC as influenced by specimen dimension and moisture, J. Mater. Civ. Eng. 2 (3) (1990) 136–146.
[24] N. Isu, S. Teramura, H. Ishida, T. Mitsuda, Influence of quartz particle size on the chemical and mechanical properties of autoclaved aerated concrete (II) fracture toughness, strength and micropore, Cem. Concr. Res. 25 (2) (1995) 249–254.
[25] B. Trunk, G. Schober, A.K. Helbling, F.H. Wittmann, Fracture mechanics parameters of autoclaved aerated concrete, Cem. Concr. Res. 29 (1999) 855–859, https://doi.org/10.1016/S0008-8846(99)00059-9.
[26] D. Ferretti, E. Michelini, G. Rosati, Cracking in autoclaved aerated concrete: Experimental investigation and XFEM modeling, Cem. Concr. Res. 67 (2015) 156–167, https://doi.org/10.1016/j.cemconres.2014.09.005.
[27] S.F. Resan, S.M. Chassib, S.K. Zemam, M.J. Madhi, New approach of concrete tensile strength test, Case Stud. Constr. Mater. 12 (2020) e00347.
[28] N.R. Devi, P.K. Dhir, P. Sarkar, Influence of strain rate on the mechanical properties of autoclaved aerated concrete, J. Build. Eng. 57 (2022), 104830.
[29] L. Małyszko, E. Kowalska, P. Bilko, Splitting tensile behavior of autoclaved aerated concrete: comparison of different specimens' results, Constr. Build. Mater. 157 (2017) 1190–1198.
[30] D. Pietras, T. Sadowski, A numerical model for description of mechanical behaviour of a functionally graded autoclaved aerated concrete created on the basis of experimental results for homogenous autoclaved aerated concretes with different porosities, Constr. Build. Mater. 204 (2019) 839–848.
[31] R. Jasiński, Ł. Drobiec, W. Mazur, Validation of selected non-destructive methods for determining the compressive strength of masonry units made of autoclaved aerated concrete, Materials (Basel). 12 (2019) 389.
[32] RILEM Recommendation, AAC13.1,, Determination of the specific fracture energy and strain softening of AAC, RILEM Technical Recommendations for the testing and use of construction materials, E & FN Spon, 1994.
[33] RILEM FMC-50, Determination of the fracture energy of mortar and concrete by means of threepoint bend tests on notched beams, Mater. Struct. 18 (1985) 287–290.
[34] JCI-S-001-2003, Method of test for fracture energy of concrete by use of notched beam, 2003.
[35] E. Brühwiler, F.H. Wittmann, The wedge splitting test, a new method of performing stable fracture mechanics tests, Eng. Fract. Mech. 35 (1-3) (1990) 117–125.
[36] Z.P. Bažant, J.-L. Le, M. Salviato, Quasibrittle fracture mechanics and size effect: a first course, Oxford University Press, 2021.
[37] Matlab. Version R2022b. Natick; Massachussetts: The MathWorks Inc., (2022).
[38] G. Papazafeiropoulos, M. Muñiz-Calvente, E. Martínez-Pañeda, Abaqus2Matlab: A suitable tool for finite element post-processing, Adv. Eng. Softw. 105 (2017) 9–16.
[39] ABAQUS Analysis Users' Manual, Dassault Systèmes Simulia Corp, Providence, RI, USA.
[40] EN 772-1, Methods of test for masonry units - Part 1: Determination of compressive strength; 2011 + A1:2015.
[41] EN 1351, Determination of flexural strength of autoclaved aerated concrete, 1998.
[42] E.W. Washburn, Note on a method of determining the distribution of pore sizes in a porous material, Proc. Natl. Acad. Sci. 7 (4) (1921) 115–116.
[43] EN 772-13, Methods of test for masonry units - Determination of net and gross dry density of masonry units (except for natural stone), 2000.
[44] J. Blaber, B. Adair, A. Antoniou, Ncorr: open-source 2D digital image correlation matlab software, Exp. Mech. 55 (2015) 1105–1122.
[45] Ł. Skarżyński, J. Kozicki, J. Tejchman, Application of DIC technique to concrete—study on objectivity of measured surface displacements, Exp. Mech. 53 (9) (2013) 1545–1559.
[46] S. Bhowmik, S. Ray, An experimental approach for characterization of fracture process zone in concrete, Eng. Fract. Mech. 211 (2019) 401–419.
[47] A. Carpinteri, Mechanics of materials and fracture mechanics (in Italian), Pitagora Editrice, Bologna, 2002.
[48] L. Mantovani, Personal communication.
[49] G. Schober, The most important aspects of microstructure influencing strength of AAC, AAC, Taylor Fr Hal. (2005) 145–153.
[50] G. Schober, Porosity in Autoclaved Aerated Concrete (AAC): A Review on Pore Structure, Types of Porosity, Measurement Methods and Effects of Porosity on Properties., in: 5th Int. Conf. Autoclaved Aerated Concr. Bydgoszcz, Poland, 14–17 Sept. 2011; pp. 39–43.
[51] N. Anders, Investigations about porosity analyzing of AAC, Ce/Papers. 2 (4) (2018) 141–145.
[52] O. Kreft, J. Hausmann, J. Hubálková, C.G. Aneziris, B. Straube, T. Schoch, Pore size distribution effects on the thermal conductivity of light weight autoclaved aerated concrete, in: 5th Int. Conf. Autoclaved Aerated Concr. Bydgoscsz, Pol., 2011: pp. 257–264.
[53] N. Narayanan, K. Ramamurthy, Structure and properties of aerated concrete: A review, Cem. Concr. Compos. 22 (2000) 321–329, https://doi.org/10.1016/S0958-9465(00)00016-0.
[54] J. Lubliner, J. Oliver, S. Oller, E. Oñate, A plastic-damage model for concrete, Int. J. Solids Struct. 25 (3) (1989) 299–326.
[55] A.-R. Hasan, D. Mohammed, Comparative assessment of commonly used concrete damage plasticity material parameters, Eng. Trans. 70 (2022) 157–181.
[56] S. Mollaei, R. Babaei Ghazijahani, E. Noroozinejad Farsangi, D. Jahani, Investigation of behavior of masonry walls constructed with autoclaved aerated concrete blocks under blast loading, Appl. Sci. 12 (2022) 8725.
[57] R.A. Iernutan, F. Babota, Numerical simulations for autoclaved aerated concrete (AAC) masonry modules reinforced with columns of disperse reinforced concrete, Procedia Manuf. 32 (2019) 908–915.
[58] J. Lu, J. Chen, K. Zhu, H. Xu, W. Zhang, Q. Deng, Experimental and numerical studies on the behaviors of autoclaved aerated concrete panels with insulation boards subjected to wind loading, Materials (Basel). 14 (2021) 7651.
[59] A. Raj, Strength enhancement of autoclaved aerated concrete (AAC) block and its masonry, Doctoral dissertation (2020).
[60] G. Castellazzi, A.M. D'Altri, S. de Miranda, F. Ubertini, An innovative numerical modeling strategy for the structural analysis of historical monumental buildings, Eng. Struct. 132 (2017) 229–248.
[61] C.G. Hoover, Z.P. Bažant, Cohesive crack, size effect, crack band and work-of-fracture models compared to comprehensive concrete fracture tests, Int. J. Fract. 187 (1) (2014) 133–143.
[62] M. Jirásek, M. Bauer, Numerical aspects of the crack band approach, Comput. Struct. 110 (2012) 60–78.
[63] L. Cedolin, S.D. Poli, I. Iori, Tensile behavior of concrete, J. Eng. Mech. 113 (3) (1987) 431–449.
[64] Z.M. Wu, H. Rong, JianJun Zheng, F. Xu, W. Dong, An experimental investigation on the FPZ properties in concrete using digital image correlation technique, Eng. Fract. Mech. 78 (17) (2011) 2978–2990.
[65] J.C. Lagarias, J.A. Reeds, M.H. Wright, P.E. Wright, Convergence properties of the Nelder-Mead simplex method in low dimensions, SIAM J. Optim. 9 (1) (1998) 112–147.